Gate-Tunable Superconductor-Semiconductor Parametric Amplifier

D. Phan,[1] P. Falthansl-Scheinecker,[1] U. Mishra,[1] W.M. Strickland,[2] D. Langone,[2] J. Shabani,[2,*]
and A.P. Higginbotham[1,†]

[1] *Institute of Science and Technology Austria (ISTA), Am Campus 1, Klosterneuburg 3400, Austria*
[2] *Center for Quantum Information Physics, Department of Physics, New York University (NYU), New York, New York 10003, USA*

(Received 1 October 2022; revised 19 February 2023; accepted 17 May 2023; published 9 June 2023)

We build a parametric amplifier with a Josephson field-effect transistor (JoFET) as the active element. The resonant frequency of the device is field-effect tunable over a range of 2 GHz. The JoFET amplifier has 20 dB of gain, 4 MHz of instantaneous bandwidth, and a 1-dB compression point of −125.5 dBm when operated at a fixed resonance frequency.

DOI: 10.1103/PhysRevApplied.19.064032

I. INTRODUCTION

Quantum limited amplifiers are, for many experimental platforms, the first link in the quantum signal-processing chain, allowing minute signals to be measured by noisy classical electronics [1–3]. Whereas later parts of the chain are dominated by semiconductor-based devices, the quantum limited step is usually performed using metallic superconductors [4–12], although very recently quantum limited amplifiers have been demonstrated using graphene weak links [13,14]. Aluminum-oxide-based tunnel junctions have proven to be more reliable and stable than any other platform, due to the formation of pristine Al-AlO$_x$ interfaces through the natural oxidization of Al.

A comparable natural, coherent, and scalable interface between a superconductor and a semiconductor has only recently been introduced in the form of Al-InAs hybrid two-dimensional electron gas heterostructures [15–17]. Josephson junctions fabricated on these materials yield a voltage-controllable supercurrent with highly transparent contacts between Al and InAs quantum wells [18–20]. Al-InAs has recently been instrumental in exploring topological superconductivity [21–24], mesoscopic superconductivity [25], and voltage-tunable superconducting qubits [26]. Al-InAs hybrids have also been used to demonstrate magnetic-field-compatible superconducting resonators [27] and qubits [28,29]. There has also been impressive recent progress on realizing all-metallic field-compatible parametric amplifiers [30–32].

More broadly, the inherent scalability of semiconductors has motivated a great deal of research on quantum applications, including the scalable generation of quantum control signals [33–36], amplification [37], and the processing of quantum information [26,38] at fault-tolerant thresholds [39–43].

Here, we introduce Al-InAs as the basis for quantum signal-processing devices. We demonstrate a gate-tunable parametric amplifier using an Al-InAs Josephson field-effect transistor (JoFET) as the active element. Our device has a resonant frequency that is tunable over 2 GHz via the field effect. In the optimal operating ranges, the JoFET amplifier has 20 dB of gain with a 4-MHz instantaneous bandwidth. The gain is sufficient for integration into a measurement chain with conventional semiconductor amplifiers. Accordingly, we find that the amplifier dramatically improves signal recovery when used at the beginning of a typical measurement chain. We quantify noise performance by calibrating our classical measurement chain, measuring the insertion loss of all components used to connect the chain to the JoFET amplifier, and then referring the measured noise to the JoFET input. This procedure suggests that the input-referred noise of the JoFET amplifier approaches the limits imposed by quantum mechanics, although a calibrated noise source at device input is needed to definitively verify quantum limited performance. Motivated by the successful operation of Al-InAs hybrid microwave circuits at large magnetic fields [27–29], the magnetic field compatibility is investigated. The performance is noticeably degraded by even small 15-mT parallel magnetic fields. In contrast to metallic superconducting amplifiers, our platform is gate tunable and it is natural to use it as a detector for voltages from a high-impedance source.

II. DEVICE DESIGN

The JoFET amplifier is implemented as a half-wave coplanar-waveguide (CPW) resonator with a gated

---

[*] js10080@nyu.edu
[†] andrew.higginbotham@ista.ac.at

superconductor-semiconductor hybrid Josephson field-effect transistor positioned at the voltage node [Fig. 1(a)]. The ground planes of the device are formed from 50-nm thin-film Nb with 1-μm^2 flux-pinning holes near the edges to improve the magnetic field resilience [44,45]. The entire center pin of the resonator is made of a Al-InAs heterostructure, defined by chemical etch. The JoFET is defined by selective removal of the Al, followed by atomic layer deposition (ALD) of alumina, and finally an electrostatic gate is defined using electron-beam lithography and Au evaporation. Large Au chip-to-chip bond pads are also codeposited in the final step to improve the wire-bonding yield. The characteristic impedance of the CPW is designed to be near 50 Ω, with a 25-μm-wide center-conductor width and a 16-μm gap to the ground plane. The device is capacitively coupled to an open 50-Ω transmission line, which forms the only measurement port.

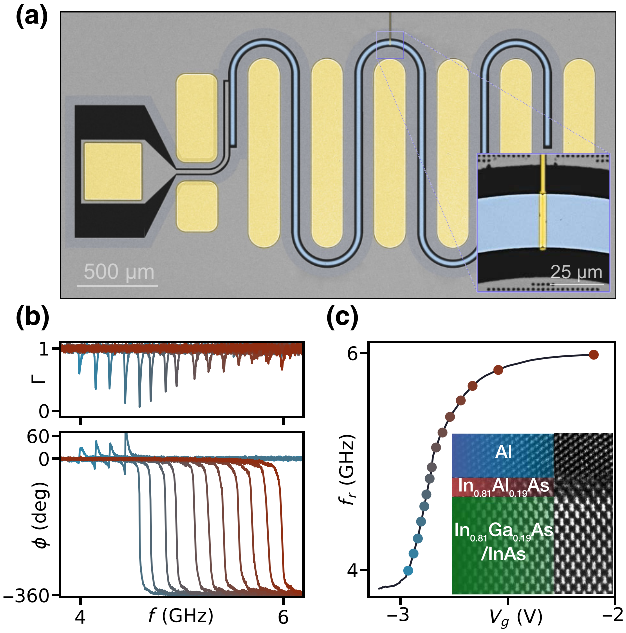

FIG. 1. The device and frequency modulation via the field effect. (a) A false-colored image of the device (InP substrate dark gray, Nb light gray, aluminum light blue, Au yellow). A feed line (left) capacitively couples to the resonator, which is formed from an Al-InAs semiconductor heterostructure. The inset shows an enlargement of the JoFET and the electrostatic gate. (b) The reflected signal magnitude Γ (top) and phase ϕ (bottom) versus the signal frequency f at 15 different gate voltages, sampled at equally spaced resonant frequencies from 4 GHz to 6 GHz. The trace colors correspond to the point colors in (c). This shows the shift of the resonant frequency with decreasing (more negative) gate voltage. (c) The resonant frequency f_r as a function of the gate voltage V_g. The dot colors correspond to the trace colors in (b). The inset shows a cross-section transmission electron micrograph at the interface of the Al thin film and the InAs quantum well. The contrast and brightness have been enhanced for clarity.

We target a geometric resonant frequency of approximately 6 GHz for compatibility with the standard 4–8 GHz band used in circuit quantum electrodynamics experiments. In designing the circuit, it is important to account for the kinetic inductance of the Al-InAs heterostructure, which in previous work has caused a 20% reduction in the circuit resonant frequency [27]. The device is therefore designed with a geometric resonant frequency of 7.2 GHz, corresponding to a CPW resonator length of 8 mm. We do not directly measure the kinetic contribution for this heterostructure growth, although we note that the Al is slightly thicker than the growth used in Ref. [27], which should result in a relatively higher resonant frequency for the devices in this work.

The external coupling κ_{ex} and the critical current I_c determine the operating bandwidth and dynamic range of the amplifier [46]. While κ_{ex} can be estimated from the circuit geometry, I_c is more subtle, because it depends on material details. Based on independent transport tests, we find that a JoFET with a width of 25 μm has an expected critical current of 10 μA at positive gate voltages. During design, we use Ref. [46] to estimate that this critical current should yield a Kerr nonlinearity on the order of a few kilohertz. A more detailed discussion of the Kerr nonlinearity for our geometry and its relationship to critical current is given in Sec. IV. Based on the dynamic range calculation in Ref. [46], a 1-dB compression point of a few photons is expected when operating with 20 dB of gain.

III. GATE TUNABILITY

The complex microwave reflection coefficient $R = \Gamma e^{i\phi}$ of a small incident signal, where Γ is the magnitude and ϕ is the phase, is measured from the sample in a dilution refrigerator with a standard measurement chain, including a cryogenic commercial high-electron-mobility-transistor (HEMT) amplifier. For large (more positive) gate voltages, the measured reflection coefficient displays a small dip in magnitude and a 360° winding of phase, signaling that the resonator is strongly coupled to the measurement port and that dissipation is weak [Fig. 1(b)]. Indeed, fitting the reflection coefficient to a one-port model gives an external coupling efficiency $\kappa_{\mathrm{ex}}/\kappa_{\mathrm{tot}} = 0.83$ at zero gate voltage.

The application of a negative gate voltage results in dramatic changes in the resonator frequency [Fig. 1(b)], indicating that the JoFET contributes a gate-tunable inductance to the resonator. The resonant frequency can be tuned over more than 2 GHz of bandwidth [Fig. 1(c)], exhibiting weak voltage dependence at extremal values, reminiscent of a transistor reaching pinch-off at negative voltage and saturation at positive voltage.

The internal dissipation rate κ_i and the external coupling rate κ_{ex} also evolve with the gate voltage. Near the JoFET pinch-off, κ_i increases sharply and κ_{ex} decreases over the

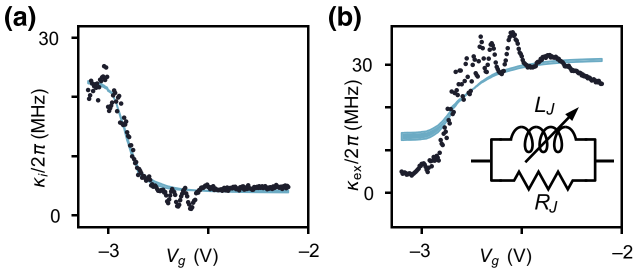

FIG. 2. The circuit model. The (a) internal loss rate κ_i and (b) external coupling $\kappa_{\rm ex}$ versus the gate voltage V_g. Experimental data are indicated by black points, and the results of parallel a *RL* model calculated for a range of bare resonant frequencies, $f_0 = 6.00$–6.45 GHz, are indicated by the blue shaded region. The inset shows the proposed JoFET linear-equivalent circuit, consisting of tunable inductance L_J and fixed shunt resistance R_J in parallel.

same range [Figs. 2(a) and 2(b)]. The net effect is therefore a decrease in coupling efficiency near pinch-off, which limits the usable frequency range of the JoFET amplifier.

A plausible origin of the increase in κ_i is dissipation in the JoFET region. To test this hypothesis, we consider a minimal model of the JoFET as a parallel resistor R_J and inductor L_J [Fig. 2(b), inset] and introduce an effective resistance $R_J/(\Delta\overline{u})^2$, where $\Delta\overline{u}$ is the normalized flux drop across the resistor. The Josephson inductance and flux drop can be inferred from the measured resonant frequency if the bare-circuit parameters without the Josephson junction are known (see Appendix C). In our case, the bare-circuit resonance is not precisely known because we do not characterize the heterostructure kinetic inductance for this particular material growth. We therefore model a range of possible bare resonant frequencies f_0. The lower value of 6 GHz is taken from the resonant frequency at high gate voltage and the upper value of 6.45 GHz is chosen to qualitatively match our measured Kerr nonlinearities, to be discussed later. The high-range value corresponds to a 10% reduction from the designed geometric resonance of 7.2 GHz, which, as one would expect, would imply that the current heterostructures have less kinetic inductance than those in our earlier studies on structures with thinner Al [27].

The fitting of κ_i to the circuit model results in agreement with the data, with a best-fit shunt resistance $R_J = 15 \pm 2$ kΩ, where the uncertainty is derived from the possible range in f_0. Based on this agreement, we conclude that the junction indeed introduces dissipation to the circuit, with the practical effect of limiting performance at high inductances. The microscopic origin of this dissipation is not understood. Candidate explanations are coupling to a lossy parasitic mode associated with the normal-conducting (Au) electrostatic gate or a mechanism that is intrinsic to the Al-InAs material system.

Turning now to external coupling, the simple *RLC* model captures the gate dependence of $\kappa_{\rm ex}$ at a qualitative level [Fig. 2(b)], although the observed gate dependence quantitatively exceeds theoretical expectations. This discrepancy may reflect the role of extra capacitance in the JoFET region introduced by the electrostatic gate, which is not accounted for in the model.

IV. NONLINEARITIES AND AMPLIFICATION

In addition to tunable inductance, the presence of the JoFET imparts a power-driven nonlinearity to the resonator [46]. Measurement of the reflected phase as a function of the signal frequency and power reveals that the resonant frequency smoothly decreases with increasing input power $P_{\rm in}$ [Fig. 3(a)]. The output power from microwave sources is related to the resonator input power

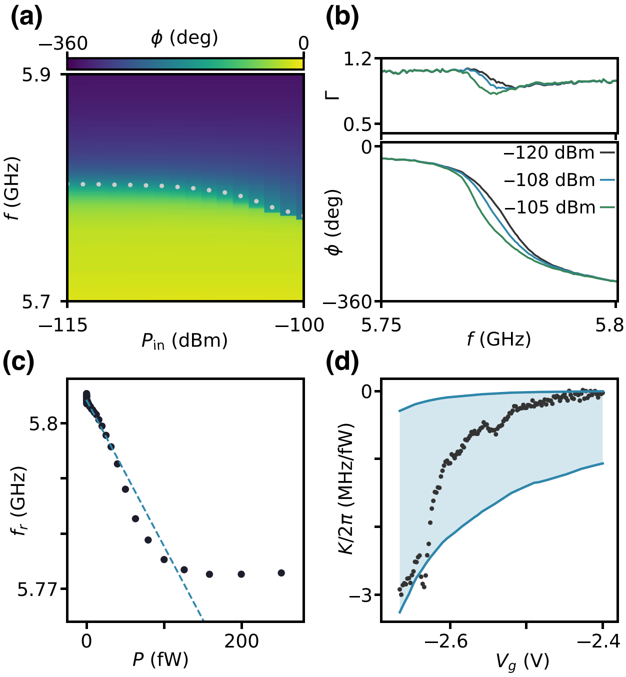

FIG. 3. The nonlinear response. (a) The reflected signal phase ϕ versus the power at resonator input $P_{\rm in}$ and frequency f. The white dots indicate the resonant frequencies f_r. (b) The reflected magnitude Γ (top) and phase ϕ (bottom) versus f at different input powers: low (black), medium (blue), and close to critical power (green). (c) The estimation of Kerr nonlinearity: resonant frequencies extracted from (a) versus the average network analyzer power applied at room temperature (dots). The slope of the linear fit (dashed line) gives an estimate of the Kerr coefficient. (d) The measured gate-dependent Kerr coefficient (black dots) and the expected value from the parallel *RL* model for a range of bare resonance frequencies $f_0 = 6.00$–6.45 GHz (blue region). The Kerr coefficient is expressed as shift per input power from the vector network analyzer (VNA) at the resonator input. Compared to (c), a different data set is used.

by an estimated total attenuation of 110 dB for all measurements. The downward shift in the resonant frequency is accompanied by "sharpening" of the phase response [Fig. 3(b)]. A downward shift in the resonant frequency and an alteration in line shape are key qualitative signatures of the required Kerr nonlinearity K, which is useful for parametric amplification. The Kerr nonlinearity is estimated by measuring the change in resonant frequency per incident power in the low-power limit, as shown by the linear fit in Fig. 3(c). Following this procedure at different gate voltages reveals that the nonlinearity is tunable with the voltage, increasing in magnitude as the gate voltage is decreased [Fig. 3(d)], which qualitatively mirrors the decrease in the circuit resonant frequency observed in Fig. 1(c). To make the relationship between the observed Kerr nonlinearity and the circuit parameters more concrete, we estimate the expected Kerr nonlinearity based on our circuit model, using the formula for a low-transmission Josephson junction (shown in Fig. 3(d); for details, see Appendix F). Unlike the case of linear circuit parameters, the uncertainty in the bare-circuit resonance frequency ($f_0 = 6.00$–6.45 GHz) translates into many orders of magnitude of uncertainty in the Kerr nonlinearity, reflecting the fact that the Kerr nonlinearity is a fourth-order effect. Despite these challenges, our estimate indicates that the magnitude of the Kerr nonlinearity that we observe is compatible with the circuit model considering this range of resonant frequencies. It is important to note that the formula with which we compare is valid only for low-transparency Josephson junctions, which is not the case for our system [19,47]. If the bare-circuit resonance was accurately known, a more complete treatment could possibly infer the true junction transparency based on the observed Kerr nonlinearity.

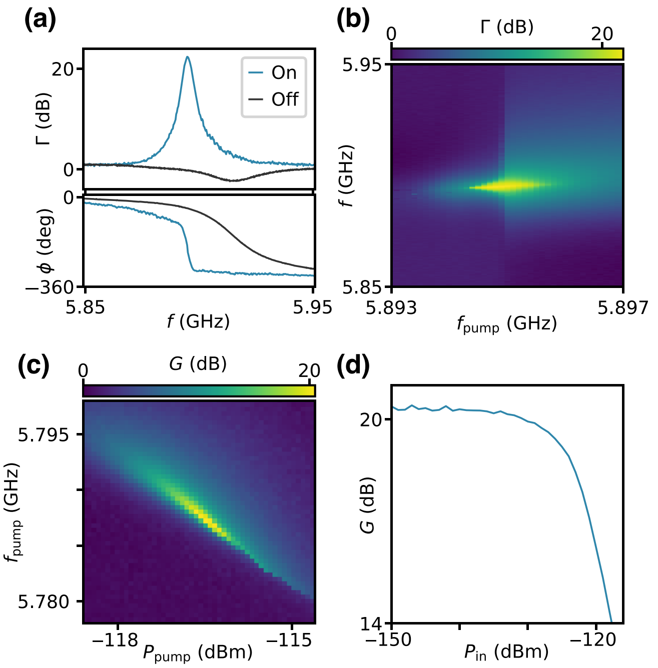

FIG. 4. The parametric gain. (a) The reflected signal magnitude Γ and phase ϕ measured as a function of the signal frequency f from the bare resonator (black) and the pumped resonator (blue). (b) Γ measured as a function of the pump frequency f_{pump} and the signal frequency f. The pump power is fixed slightly below the critical pump power at which the system bifurcates. For (a) and (b), $V_g = -2.5$ V. (c) The gain G inferred from the maximal reflected amplitude measured as a function of the pump power P_{pump} and pump frequency f_{pump}, revealing line of maximum gain. $V_g = -2.55$ V. (d) The gain G measured as a function of the signal power at device input P_{in}. $V_g = -2.35$ V, $f_{\text{pump}} = 5.942$ GHz, and the signal-pump-detuning $\delta f = 1$ MHz and remains within the 3.6-MHz instantaneous amplification bandwidth.

Parametric amplification is generated by applying a strong pump tone that is red detuned from the bare resonant frequency, in the vicinity of the phase "sharpening" features already identified close to the critical power [Fig. 3(b)]. The measurement of scattering parameters with a weak probe signal reveals in excess of 20 dB of gain with a 4-MHz bandwidth and a sharp phase response typical of a parametric amplifier [Figs. 4(a) and 4(b)]. Modest detunings in the pump frequency do not substantially affect the amplifier response but for large deviations the gain decreases toward unity [Fig. 4(b)]. Measurement of the amplifier gain G as a function of the pump frequency f_{pump} and input power P_{pump} reveals a continuous region of maximum gain with an easily identifiable optimum operating region, as expected for a parametric amplifier [Fig. 4(c)]. The gate voltages used for the gain optimization and measurement shown in Figs. 4(a) and 4(b) and in Figs. 4(c) and 4(d) are different due to gate instability, hysteresis, and shifts between cool-downs. These particular data sets are taken weeks apart, separated by many wide-range gate voltage sweeps, and in different cool-downs. Typically, after changing the gate voltage by a large amount (on the scale of volts), it takes 15 min for the resonance to stabilize and we find that there is hysteresis after large sweeps. In general, the resonant frequency remains stable for circa 1 h, which is sufficient for our gain and noise measurements. After approximately 1 h, we often find measurable changes in amplifier gain and noise performance due to resonant frequency drifts, which could be compensated by reoptimization of the pump frequency and amplitude. We emphasize that the drifts in the resonant frequency over this time period are much smaller than the line width but still noticeable when operating at high gain. We anticipate that optimization of the gate dielectric can greatly improve stability in future devices.

The power-handling capability of the amplifier is quantified by measuring the gain for different signal powers [Fig. 4(d)]. At very low input signal power, the gain saturates at 20.3 dB [Fig. 4(d)]. Large input powers cause the amplifier gain to decrease, giving a 1-dB compression point at an input power of −125.5 dBm [Fig. 4(d)]. The gain and instantaneous bandwidth are comparable to those of early parametric amplifiers based on metallic Al-AlO$_x$ Josephson junctions [7,8,48]. The frequency tunability of our resonator is also comparable to those of early parametric amplifiers [7], although we do not demonstrate tunable amplification, which would currently be limited to the low-loss frequencies (see Figs. 1 and 2). The 1-dB compression point is only slightly lower than those of some early parametric amplifiers (two times below Ref. [49]) but orders of magnitude below modern implementations [10,11]. Both the resonator loss and the compression point need to be significantly improved for this amplifier to be practically useful. In contrast to a recently demonstrated semiconductor parametric amplifier with 3 dB of gain [37], our device has sufficient gain (20 dB) to overwhelm the noise of later parts of the measurement chain.

Quantum signals typically consist of few photons, making it crucial to achieve noise performance near the quantum limit. To assess the noise performance of the JoFET amplifier, a weak pilot signal is measured first with a commercial HEMT amplifier and then with parametric gain activated [Fig. 5(a)]. The JoFET amplifier dramatically improves the signal-to-noise ratio (SNR) of the pilot-signal measurement. Our calibration procedure, described in the next paragraph and in Appendix H, gives an indication that the total input-referred noise of the JoFET amplifier and subsequent measurement chain approaches the limits placed by quantum mechanics of one photon from nondegenerate amplification [2,3]. However, a definitive check of these results would require a calibrated noise source at the device input. The excess noise in the device is consistent with expectations based on resonator loss and finite gain [Fig. 5(a), purple tick], as derived from input-output theory in Appendix I.

This noise measurement is carefully calibrated by varying the temperature of the mixing-chamber stage of the dilution refrigerator and measuring the noise at various frequencies with the JoFET amplifier off [Fig. 5(b)]. In the high-temperature limit, the output noise is linear in temperature, with an intercept that reflects the added noise of the chain referred to the mixing-chamber (MC) plate, giving $T_{H,\mathrm{MC}} = 1.61$ K at the JoFET operating frequency. At low temperature, input-referred noise saturates. Calibration over a wide range of frequencies reveals that noise saturation is pronounced only for high frequencies, consistent with the expected behavior for quantum fluctuations [3]. This provides evidence that quantum fluctuations are faithfully resolved by our measurement chain. To find the noise referred to the JoFET input, T_{in}, we measure the insertion loss of all the components in between the JoFET input and the mixing-chamber plate and use these values to refer the noise spectra to the device input (see Appendix H). This calibration procedure counts resonator and sample-holder insertion loss against the performance of the JoFET amplifier, resulting in a noise temperature that represents the JoFET added noise referred to its input, which is a suitable quantity for characterizing the JoFET as a stand-alone device. It is not a measurement of total

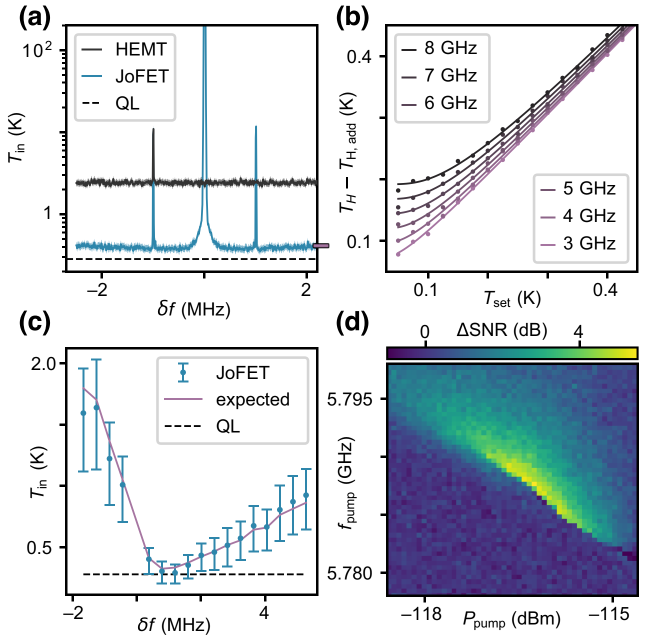

FIG. 5. The noise performance. (a) The total noise temperature referred to the JoFET input T_{in}, measured in the presence of a weak pilot tone, as a function of the detuning frequency from the pump, δf. Pump off (HEMT, black) and pump on (JoFET, blue) are shown, in comparison with the quantum limit at this frequency (0.285 K, QL, dashed). $V_g = -2.35$ V. The expected noise performance [Eq. (I6)] is indicated by a purple tick on the right-hand axis. In the JoFET data, the blue-detuned idler and the zero-detuned pump are also visible. The bands represent the propagated uncertainty from cavity parameters, insertion-loss measurements, and HEMT-noise calibration. Note that here the HEMT data are referred to the cavity input, not the HEMT input. (b) The added noise of a chain without the JoFET, referred to the HEMT input. The difference between the total noise temperature T_H and the HEMT added noise $T_{H,\mathrm{add}}$, measured as a function of the mixing-chamber temperature set point T_{set}. The lines represent unity slope due to Johnson-Nyquist noise, corrected for the presence of vacuum fluctuations, which dominate at low temperature and high frequency [3]. (c) T_{in} measured as a function of the pump-signal detuning δf by varying the pump frequency with the signal frequency fixed (blue markers). The purple line is the expected noise performance from Eq. (I6) and the dashed line is the quantum limit at this frequency (0.278 K). One data point with a detuning of 2.7 kHz has to be removed from the data set, since the pump and signal cannot be resolved individually. The error bars represent the uncertainty propagated through from the circuit parameters and the HEMT-noise calibration. (d) The relative improvement in the signal-to-noise ratio (ΔSNR), measured as a function of the pump frequency f_{pump} and the pump power P_{pump}: the signal-pump detuning is fixed at 0.5 MHz and the signal input power is fixed at −153 dBm. For (c) and (d), $V_g = -2.55$ V.

system efficiency, which would also need to include cable and circulator losses between a specified 50-Ω load and the JoFET.

Changing the pump frequency while keeping the signal frequency fixed at 5.7839 GHz reveals that the noise performance is degraded if the pump frequency is away from the optimal operating region [Fig. 5(c)]. The change in noise performance with detuning matches the predictions of Eq. (I6) with no free parameters [Fig. 5(c), purple line], indicating that the variation in the noise performance is due to decreased gain. The level of agreement between experiment and theory in Fig. 5(c) gauges the accuracy of our noise-calibration method, although we again emphasize that a calibrated noise source is needed for a definitive noise measurement. Note that this data set is taken at a gate voltage with less resonator loss ($\kappa_{\text{ex}}/\kappa = 0.91$), so the expected noise performance is somewhat better than in Fig. 5(a), but the data do not resolve this difference due to the large propagated uncertainties in Fig. 5(c). By sweeping the pump frequency and the pump power with a fixed signal detuning, the optimum operating points of the amplifier can be extracted [Fig. 5(d)]. The operating points with the best noise performance qualitatively correspond to the regions of highest gain identified in Fig. 4(c), as expected.

V. MAGNETIC FIELD OPERATION

A general technical advantage conferred by the Al-InAs hybrid platform is compatibility with large parallel external magnetic fields [27–29]. To explore if this advantage is realized in our particular device, we steadily increase the parallel external magnetic field to 15 mT while compensating for small field misalignments with a perpendicular magnetic coil. Even with compensation, the resonator parameters evolve slightly in a magnetic field and a slight increase in loss is observed. Applying a pump tone gives an optimized gain of 10 dB [Figs. 6(a) and 6(b)]. This demonstrates parametric amplification in a modest in-plane magnetic field but far less than recently demonstrated for high-field amplifiers [30–32]. Future experiments need to improve the resonator performance in a magnetic field in order to allow a reliable noise measurement; we are unable to demonstrate quantum limited operation in a magnetic field. The most likely reason for this is the depinning of trapped flux by high pump powers. This effect can be reduced by forming the resonator center pin from a field-compatible superconductor that connects to a smaller Al-InAs microstructure, as has been done with recent field-compatible superconducting qubits [28,29].

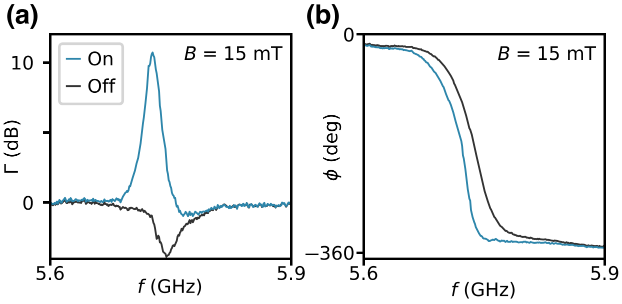

FIG. 6. The magnetic field performance. The reflected (a) magnitude Γ and (b) phase ϕ with and without the pump tone as a function of the probe frequency f in the presence of an in-plane magnetic field, $B = 15$ mT.

VI. OUTLOOK

To summarize, we demonstrate a high-performance JoFET amplifier, already obtaining performance comparable to early implementations in Al-AlO$_x$ material systems. A number of techniques are available to further improve the performance of our device. The participation factor of the superconductor-semiconductor heterostructure can be reduced drastically by working with a small mesa in the JoFET region. This would likely decrease microwave losses and allow the use of field-resilient superconductors such as Nb-Ti, which should allow operations in external magnetic fields of the order of 1 T. The number of JoFETs and the designed critical current can also be adapted to provide the target nonlinearity at milder gate voltages [46]. The device dissipation can also likely be improved by using a superconducting electrostatic gate with on-chip filters. Finally, superconducting-semiconducting hybrid material systems are being actively developed, so material-level improvements can be expected.

Our work opens up the general direction of quantum limited signal-processing devices based on semiconductors and can be expanded to devices such as modulators [48,50], circulators [51,52], or signal generators [53]. It is interesting to note that the electrostatic gate can be viewed as a receiver for high-impedance electrical signals, suggesting applications such as electrometry with an integrated quantum limited amplifier. Potential applications of electrometers include readout of spin qubits [54] and scanning-probe experiments [55,56]. Given the fact that this device uses a narrow-gap III-V semiconductor, it is also interesting to consider applications in photodetection.

The raw data and the plotting code are available in the Supplemental Material [57]. Further data are available upon reasonable request.

ACKNOWLEDGMENTS

We thank Shyam Shankar for helpful feedback on the manuscript. We gratefully acknowledge the support of the ISTA nanofabrication facility, the Miba Machine Shop, and the eMachine Shop. The NYU team acknowledges support from Army Research Office Grant No. W911NF2110303.

APPENDIX A: SAMPLE PREPARATION

The JoFET amplifier is fabricated from Al-proximitized InAs quantum well, which is grown on a semi-insulating Fe counter-doped (100) InP wafer. Patterning is performed using a Raith EBPG 5100 electron-beam-lithography system. The Josephson weak link is made by etching a trench in the aluminum layer in the commercial etchant Transene D at 50 °C for 5 s. The trench is designed to be 20 nm long and 25 µm wide. Scanning electron microscopy (SEM) later shows that the trench width is about 50 nm. The superconductor-semiconductor mesa forming the center pin of the CPW resonator is formed by masking with polymethyl methacrylate (PMMA), followed by a semiconductor wet etch in a CH_3COOH-H_2O_2-H_3PO_4 mixture for 150 s at room temperature. The ground plane is constructed by evaporating Ti(5 nm) and Nb(50 nm) following a short 1-min Ar ion milling at an accelerating voltage of 400 V, with an ion current of 21 mA, in a Plassys ultrahigh-vacuum (UHV) evaporator. In the next step, the dielectric layer separating the gate and the junction is deposited using an Oxford ALD system running a thermal ALD alumina process at 150 °C in 150 cycles, which gives an approximated thickness of 12 nm. Eventually, the gate that covers just the area of the Josephson weak link is created by evaporating Ti(8 nm) and Au(80 nm) at a tilt angle of 30° with 5-rpm (revolutions per minute) planetary rotation in a Plassys high-vacuum (HV) evaporator. Due to low adhesion of the Al bond wire to the Nb ground plane, codeposited Au bond pads are used to enhance Al alloy formation during wire bonding and, hence, the chip-to-chip bond yield. All lift-off and cleaning processes are performed in hot acetone at 50 °C and isopropanol.

The schematic in Fig. 7 shows a cross section of the JoFET.

APPENDIX B: MEASUREMENTS

The sample is mounted on a copper bracket on a homemade printed circuit board. We use a Keysight model P9372A vector network analyzer (VNA) to measure the scattering parameters. A Rohde & Schwarz (R&S) model SGS100A signal generator is used to provide the pump tone. When pumping at a fixed frequency, we use the VNA to provide a small probe signal and we measure the gain profile from the reflected monotone at the probe frequency. A custom-built low-noise voltage source provides the gate bias. To achieve gain, we typically set the gate voltage to −2.5 V and sweep the VNA power until the response becomes critical. A pump tone from an R&S signal generator is injected at a power of about 1 dB below the approximated critical power and slightly above the critical frequency. The probe power from the VNA is reduced to maintain the validity of the stiff pump condition. We tune up the JoFET amplifier by sweeping the pump frequency and power in the proximity of the critical values of the nonlinear resonator and recording the maximal reflected amplitude at the VNA input. The optimal amplification configurations are then found by fine sweeping around the regions where the maximal gains are highest, the values being typically more than 20 dB. To measure the noise, we record the power spectral density from the output of the JoFET amplifier using a ThinkRF R5550 hybrid spectrum analyzer. The in-plane magnetic field and compensation are applied by a vector magnet system of the Oxford Triton fridge and the Mercury iPS power supply.

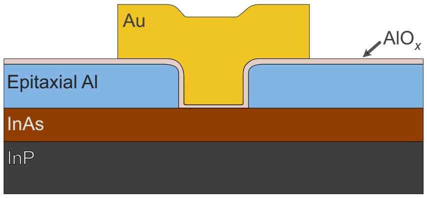

FIG. 7. A cross-section sketch of the JoFET: from bottom to top, the substrate is 500-µm-thick InP(100), the quantum well is a heterostructure denoted InAs, the superconductor is a 10-nm-thick layer of epitaxial Al, the dielectric that separates the Al and the gate is made with thermal-ALD AlO_x, and the gate is made by evaporating 80 nm of Au at a 30° tilt angle. The sketch dimensions are not to scale.

APPENDIX C: *RLC* CIRCUIT MODEL

To model the gate dependence of κ_{ex} and κ_i in Fig. 2, we find an effective lumped-element representation of the circuit and then couple it to the transmission lines following the procedure in Ref. [58].

Our circuit can be imagined as two resonators of length l and inductance per unit length L_l, capacitance per unit length C_l, and attenuation constant α, coupled through the parallel RL circuit. For a large shunt resistance, the inductance of the parallel combination is given by L_J. In this limit, the model therefore introduces dissipation without substantially altering the resonant frequency. The resonant wave vector k satisfies [59]

$$2\cot(kl) = \frac{L_J}{L_l l} kl. \tag{C1}$$

The effective capacitance is [46]

$$C_{\text{eff}} = C_l l \left(1 + \operatorname{sinc}(2kl)\right). \tag{C2}$$

This expression arises from equating the capacitive energy in both resonators $2\int_{-l}^{0} dx C_l u(x)^2$ with an equivalent lumped-element energy $C_{\text{eff}} u_i^2$, where $u(x) = -u_i \cos k_i(x+l)$ is a flux normal mode with wave vector k_i [46,59].

We do not know of an explicit treatment of dissipation in our geometry available in the literature, so we seek an effective resistance in analogy with the effective capacitance discussed above. The Rayleigh dissipation function, which entirely determines the effect of the resistance on the circuit dynamics [60], is $\Delta\dot{u}(x)^2/(2R_J)$, where Δu is the flux drop across the resistor. This has the physical interpretation of 1/2 of the dissipated electrical power. Equating the dissipation function with an effective lumped-element dissipation rate $\dot{u}_i^2/(2R_{\text{eff}})$ suggests an effective resistance $R_{\text{eff}} = R_J/(\Delta\bar{u})^2$, where $\Delta\bar{u} = 2\cos(kl)$ is the normalized flux drop across the resistor. Working in an effective lumped-element circuit model [58], we then add R_{eff} in parallel with the resonator dissipation, finding expressions for the total dissipation and coupling rates,

$$\kappa_i = \frac{\alpha l}{Z_0 C_{\text{eff}}} + \frac{1}{R_{\text{eff}} C_{\text{eff}}}, \tag{C3}$$

$$\kappa_{\text{ex}} = \frac{1}{R^* C_{\text{eff}}}, \tag{C4}$$

where $R^* = (1 + \omega_k^2 C_k^2 Z_0^2)/(\omega_k^2 C_k^2 Z_0)$ is the effective parallel resistance from the measurement port, with impedance Z_0 coupled with capacitance C_k.

To fit this model, we use the fact that $kl = (\pi/2) f/f_0$, where f_0 is the bare resonant frequency of the CPW resonator when L_J is zero. As discussed in the main text, due to our uncertainty over how much inductance the junction contributes at large gate voltage, we consider a range $f_0 = 6.00$–6.45 GHz and then extract kl directly from the measured data. We fix the characteristic impedance of the resonator as $Z_0 = 50\ \Omega \times (f_{\text{geo}}/f_0)$ based on the ratio between the designed geometric resonance frequency f_{geo} and the actual bare resonant frequency f_0, which physically originates from the kinetic inductance of the heterostructure [27]. Knowledge of kl, f_0, and Z_0 allows the effective capacitance and Josephson inductance to be calculated. Equation (C3) is fitted for α and R_J in Fig. 2(a) and Eq. (C4) is fitted for C_k.

APPENDIX D: CONVERSION FROM SIGNAL POWER TO AVERAGE INTRACAVITY PHOTON NUMBER

The average intracavity photon number n is linearly dependent on the incident power P_{in} at the input port:

$$n = \frac{1}{hf_s} \frac{4\kappa_{\text{ex}} P_{\text{in}}}{(\kappa_{\text{ex}} + \kappa_i)^2 + 4\Delta^2}. \tag{D1}$$

The input power is estimated based on the VNA power and the total attenuation A of the setup. This is used when expressing the theoretical Kerr nonlinearity as a frequency shift per input power (MHz/fW) in Fig. 3(d).

APPENDIX E: TOTAL ATTENUATION ESTIMATE

The total attenuation A between the output of the VNA and the input of the device is calculated from the noise spectrum from the measurement port with a signal tone at −43 dBm output power. The noise floor is identified with input-referred noise temperature $T_{H,\text{MC}} = 1.61$ K from the HEMT calibration measurement shown in Fig. 5(b), combined with the resolution bandwidth of the signal analyzer BW = 3.88 kHz, giving $P_{\text{noise}} = 10\log(k_B T_N \text{BW}/(1\ \text{mW})) = -160.6$ dBm. The signal is 6.3 dB above the noise floor, so its input-referred magnitude is −153 dBm. Accounting for the small −0.84 dB of loss from the (detuned) cavity then gives the total attenuation $A = -110$ dB quoted in the main text. This value is compatible with expectations based on our installed attenuators and stainless-steel cryogenic coaxial cables (estimated −66 dB) and room-temperature components (−40 dB).

APPENDIX F: KERR NONLINEARITY EXTRACTION FROM POWER SWEEP

The dependence of the resonance frequency on the input power is used to estimate the Kerr nonlinearity K similarly to Ref. [7]. The resonant frequency decreases linearly with an increasing average intracavity photon number following the Hamiltonian [46]:

$$H_{\text{JPA}} = \hbar\left(\tilde{\omega}_0 + \frac{K}{2}\left\langle A^\dagger A\right\rangle\right) A^\dagger A. \tag{F1}$$

The slope of the line in Fig. 3(c) measures $K/2$.

For low-transmission Josephson junctions, there is a fixed relationship between the Josephson energy E_J and the Kerr nonlinearity [46,59],

$$\hbar K = -\frac{e^2}{2C_{\text{eff}}} \frac{L_{\text{eff}}}{L_J} \Delta\bar{u}^4, \tag{F2}$$

where $L_{\text{eff}} = (4\pi^2 f_r^2 C_{\text{eff}})^{-1}$ is the effective inductance and $\Delta\bar{u} = 2\cos(kl)$ is the normalized flux drop across the junction. We use this formula in Fig. 3(d).

APPENDIX G: JoFET AMPLIFIER DESIGN

The CPW resonator is designed to have a characteristic impedance of 50 Ω with the center-conductor width and gap of 25 μm and 16 μm, respectively. The resonator length is chosen so that the target resonant frequency of 6 GHz will be achieved at base temperature. To account for the kinetic inductance of the 10-nm-thick Al layer, the geometric resonant frequency is designed to be 7.2 GHz, so that the resulting resonance will drop to 6 GHz based on previous fabrication experience. The kinetic inductance of the Al film fluctuates from device to device, presumably due to uncontrolled oxidation of the Al. The JoFET is designed for a maximal critical current of 10 μA. The designed dimensions are chosen based on our previous lithography tests and critical current measurements, where a sheet critical current density of 0.38 μA/μm is achieved.

APPENDIX H: JoFET INPUT NOISE REFERRAL

The temperature sweep in Fig. 5(b) is used to refer HEMT noise to the mixing-chamber plate [Fig. 8, point $\diamond$]. Noise is then referred to the device input [Fig. 8, point $\star$] by measuring the transmission η of the components in the signal path: the circulators, coaxial cables, sample board, and device [7]. We model this total loss as being from a beam splitter with efficiency η [61].

The noise referred to point $\diamond$, $S_\diamond$, is related to the real input noise at point $\star$, $S_{\star,\text{in}}$, according to $S_\diamond = \eta S_{\star,\text{in}} + (1-\eta)V + T_{H,\text{MC}}$, where the second term represents the introduction of vacuum noise V by loss. The total noise referred to point $\star$ is then

$$S_\diamond/\eta = S_{\star,\text{in}} + \frac{1-\eta}{\eta}V + \frac{1}{\eta}T_{H,\text{MC}}, \tag{H1}$$

which in the special case of vacuum-noise input gives $(T_{H,\text{MC}} + V)/\eta$.

There are two important cases in the experiment: the measurement with the JoFET amplifier *off* [Fig. 5(a), black line] and the measurement with the JoFET amplifier *on* [Fig. 5(a), blue line]. In the *off* state, the pilot tone is not on resonance with the cavity but still experiences a small loss $1-\eta_{c,\text{off}}$ because of finite detuning. In addition to cavity loss, there is an imperfect system transmission η_s from the components between points $\star$ and $\diamond$: the sample board, the circulators, and the coaxial cables. This results in a net transmission in the *off* state of

$$\eta_{\text{off}} = \eta_{c,\text{off}}\eta_s. \tag{H2}$$

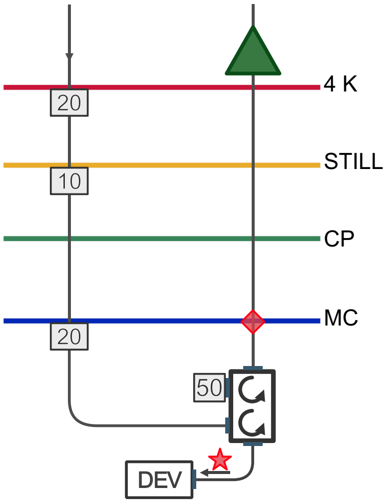

FIG. 8. A schematic of the insertion loss calibration. Noise referred to the point shown as a diamond ($\diamond$) is referred to the device input (shown as $\star$) by measuring the cold insertion loss of each component. Stainless-steel coaxial cables and 50 dB of additional attenuation thermalize signals on the input and niobium coaxial cables are used between the 4 K and MC stages on the readout chain.

In the *on* state, there is a net gain G from the device and the same system loss, so the net transmission in the *on* state is

$$\eta_{\text{on}} = G\eta_s. \tag{H3}$$

Note that according to this definition, G is the net gain of the amplifier including any cavity losses when it is *on*.

Input-referred noise is found by substituting into Eq. (H1) $\eta = \eta_{\text{on}}$ in the *on* case and $\eta = \eta_{\text{off}}$ in the *off* case. Below, we discuss how the three key parameters, η_s, $\eta_{c,\text{off}}$, and G, are measured.

We find η_s by measuring the transmission through our cryostat at a base temperature < 0.05 K with and without the cable-circulator combination [0.6 dB from Fig. 9] and we also directly measure the sample-holder insertion loss to be 0.2 dB at liquid-nitrogen temperatures. These losses combine to give our system loss $\eta_s = 0.8$.

We find $\eta_{c,\text{off}} = 0.87$ from measured scattering parameters in the same configuration, taking into account the detuning of the pilot from circuit resonance. We emphasize that this number only includes a contribution from the off-resonant insertion loss of the circuit but not any system components such as the sample holder.

We find the gain G by comparing the height of the pilot tone in the *off* state, $P_{\text{off}} = \eta_{\text{off}}P_{\star,\text{in}}$, and in the *on* state, $P_{\text{on}} = \eta_{\text{on}}P_{\star,\text{in}}$, for a fixed pilot power $P_{\star,\text{in}}$. Using Eqs. (H2) and (H3), we find the gain at the pilot frequency:

$$G = \eta_{c,\text{off}}\frac{P_{\text{on}}}{P_{\text{off}}}. \tag{H4}$$

The frequency dependence of the gain is found from scaling a Lorentzian fit of the measured noise spectrum.

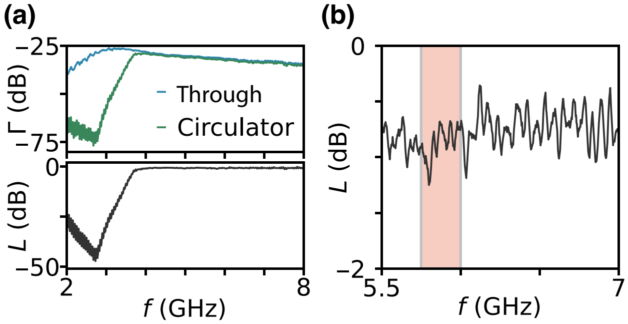

FIG. 9. The calibration trace at base temperature in a dilution refrigerator. (a) Upper plot: the frequency-dependent transmission via a through cable (blue) and via the circulator and cables used for the measurements in the main text (green). Lower plot: the frequency-dependent insertion loss L calculated by the difference of the two traces in the upper plot. (b) An enlargement of the insertion loss over a relevant frequency region. To estimate the insertion loss in our experiment, we average over the frequency range 5.75–6 GHz (shaded region), finding an insertion loss of 0.6 ± 0.1 dB, where the uncertainty is from the standard deviation over the same range.

APPENDIX I: EXPECTED NOISE PERFORMANCE

The quantum limit for phase-insensitive amplification is $2V$ of input-referred added noise, where $V = hf/2$ is the noise due to zero-point vacuum fluctuations [2]. Losses and finite gain cause deviations from this limit. Here, we determine the expected noise performance of our JoFET amplifier accounting for these effects.

We begin with the input-output relations for a Josephson parametric amplifier with input mode $a_{\mathrm{in},\Delta}$ and output mode $a_{\mathrm{out},\Delta}$ at a detuning Δ from the pump frequency [46],

$$\begin{aligned} a_{\mathrm{out},\Delta} &= g_S a_{\mathrm{in},\Delta} + g_I a^{\dagger}_{\mathrm{in},-\Delta} \\ &\quad + \sqrt{\frac{\kappa_i}{\kappa_{\mathrm{ex}}}}(g_S+1) b_{\mathrm{in},\Delta} + \sqrt{\frac{\kappa_i}{\kappa_{\mathrm{ex}}}} g_I b^{\dagger}_{\mathrm{in},-\Delta}. \end{aligned} \tag{I1}$$

The bath mode $b_{\mathrm{in},\Delta}$ is required by the fluctuation-dissipation relation in the presence of nonzero loss. The complex signal gain g_S is identically the scattering parameter Γ and the idler gain g_I ensures that $a_{\mathrm{out},\Delta}$ satisfies bosonic commutations relations [3]. These commutation relations imply that

$$\left(1 + \frac{\kappa_i}{\kappa_{\mathrm{ex}}}\right)|g_I|^2 = |g_S|^2 - 1 + \frac{\kappa_i}{\kappa_{\mathrm{ex}}}|g_S+1|^2. \tag{I2}$$

Assuming, for convenience, that the bath and idler modes are in their ground state with power spectral density V, the output spectral density of the JoFET amplifier S_J can be related to the input spectral density $S_{\star,\mathrm{in}}$ using Eq. (I1):

$$S_J = S_{\star,\mathrm{in}}|g_S|^2 + V\frac{\kappa_i}{\kappa_{\mathrm{ex}}}|g_S+1|^2 + V\left(1+\frac{\kappa_i}{\kappa_{\mathrm{ex}}}\right)|g_I|^2. \tag{I3}$$

The elimination of g_I using Eq. (I2) and input referral by dividing out the gain gives $S_J/|g_S|^2 = S_{\star,\mathrm{in}} + S_{\mathrm{add},J}$, where the input-referred noise added by the JoFET amplifier is

$$S_{\mathrm{add},J} = V + 2V\frac{\kappa_i}{\kappa_{\mathrm{ex}}}\frac{|g_S+1|^2}{|g_S|^2} - \frac{V}{|g_S|^2}. \tag{I4}$$

This expression represents the input-referred added noise of the JoFET amplifier accounting for both finite gain and resonator loss. The first term is the quantum limit on added noise. The second term gives corrections due to resonator loss. The final term gives a loss-independent correction for finite gain. In the high-gain limit, Eq. (I4) reduces to a limiting value

$$S_{\mathrm{add},J} \approx V + \frac{2\kappa_i}{\kappa_{\mathrm{ex}}}V, \tag{I5}$$

which can be interpreted as the quantum limit plus unavoidable vacuum fluctuations arising from loss at the cavity input. Equation (I5) is sometimes referred to as the device quantum limit [62].

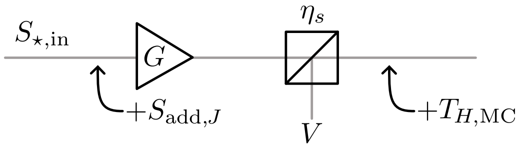

FIG. 10. The noise model for estimating the expected performance. The input noise $S_{\star,\mathrm{in}}$ is amplified by a JoFET amplifier with input-referred added noise $S_{\mathrm{add},J}$ given by Eq. (I4) with on-resonant gain $g_S = \sqrt{G}$, followed by system losses modeled as a beam splitter with efficiency η_S and a classical measurement chain with added-noise temperature $T_{H,\mathrm{MC}}$.

As a check of Eq. (I4), one can substitute $g_S = (\kappa_{\mathrm{ex}} - \kappa_i)/\kappa$, corresponding to the case where the amplifier is off and noise is measured at cavity resonance, and $S_{\star,\mathrm{in}} = V$, corresponding to vacuum-noise input. In this case, one finds that the output noise is also vacuum, $S_{\mathrm{JPA}} = |g_S|^2(V + S_{\mathrm{add,JPA}}) = V$, as expected.

To include the effect of system losses η_S followed by our classical chain with temperature $T_{\mathrm{HM},C}$, we combine Eq. (I4) with a simple beam-splitter noise model, as indicated in Fig. 10. The total input-referred noise of the model at small detunings where the gain is real, $g_S = \sqrt{G}$, is

$$S_{\star,\mathrm{in}} + S_{\mathrm{add,J}} + \frac{1-\eta_s}{\eta_s G}V + \frac{T_{H,\mathrm{MC}}}{\eta_s G}. \tag{I6}$$

The insertion of $S_{\star,in} = V$ along with the measured device parameters and the system loss from Appendix H gives a total expected input-referred noise of 0.41 K for the data in Fig. 5(a) (indicated by the purple tick on the right-hand axis). Equation (I6) is also used to calculate the expected noise performance in Fig. 5(c).

APPENDIX J: REPEATABILITY OF CALIBRATION DATA

The reproducibility of our circulator and cable insertion-loss measurements is key for the calibration described in Appendix H. To check the stability of our method, more than 1 week after calibrating we removed the circulators and cables and repeated our through-calibration measurement [Fig. 11(a)]. The two measurements differ by less than 0.2 dB over the relevant frequency range, with an average difference of 0.13 dB. Since our calibration occurs over a time span of a few days, we interpret the 0.2 dB value measured over 1 week as a conservative bound on drifts during our calibration procedure. We therefore include an additional 0.2 dB of uncertainty in the error bars in Figs. 5(a) and 5(c).

The calibrated components are inserted or removed via a bottom-loading exchange mechanism, which avoids having to thermally cycle the whole system. We suspect that

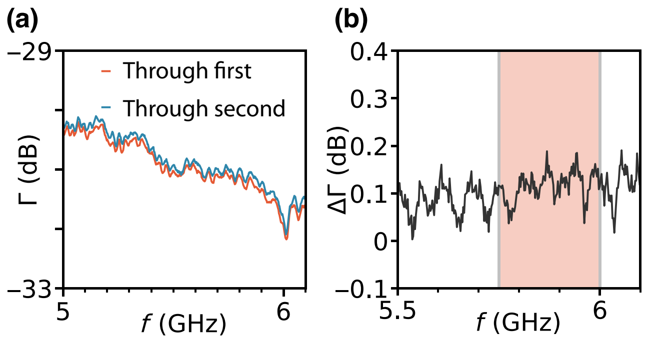

FIG. 11. The repeatability of the calibration data at base temperature in the dilution refrigerator. (a) The frequency-dependent transmission magnitude via a through cable from two different measurements. (b) The frequency-dependent difference of the transmission from the two traces in (a). The difference is smaller than 0.2 dB in magnitude over the relevant (shaded) frequency range and is on average 0.13 dB.

this feature greatly improves the reproducibility of our method.

APPENDIX K: SUMMARY OF DATA SETS

Here, we summarize the different data sets used in this work to facilitate their comparison:

(1) *Circuit characterization*. A single continuous data set is used for Figs. 1 and 2. A single data set is used to demonstrate circuit nonlinearities in Figs. 3(a)–3(c). The nonlinearity is then characterized as a function of the gate voltage in another data set in Fig. 3(d). We check that the circuit resonant frequencies in Fig. 3(d) are compatible with those in Fig. 1(c).

(2) *Amplifier characterization*. A single data set is used to show the typical dependence of the scattering parameters on the pump power in Figs. 4(a) and 4(b). Consecutive data sets at a nearby (50 mV lower) gate voltage are then used to characterize the dependence of the gain [Fig. 4(c)] and the signal-to-noise ratio [Figs. 5(c) and 5(d)] on the pump power and frequency. The key amplifier metrics of the input-referred noise [Fig. 5(a)] and the compression point [Fig. 4(d)] are measured consecutively. Noise is measured first and the compression point is measured at the same gate voltage approximately 5 h later. The HEMT calibration in Fig. 5(b) is performed on the following day.

(3) *Magnetic field data*. The two traces shown in magnetic field [Figs. 6(a) and 6(b)] are at identical gate voltages and are taken under the same conditions.

[1] H. A. Haus and J. A. Mullen, Quantum noise in linear amplifiers, Phys. Rev. **128**, 2407 (1962).

[2] C. M. Caves, Quantum limits on noise in linear amplifiers, Phys. Rev. D **26**, 1817 (1982).

[3] A. A. Clerk, M. H. Devoret, S. M. Girvin, Florian Marquardt, and R. J. Schoelkopf, Introduction to quantum noise, measurement, and amplification, Rev. Mod. Phys. **82**, 1155 (2010).

[4] B. Yurke, L. R. Corruccini, P. G. Kaminsky, L. W. Rupp, A. D. Smith, A. H. Silver, R. W. Simon, and E. A. Whittaker, Observation of parametric amplification and deamplification in a Josephson parametric amplifier, Phys. Rev. A **39**, 2519 (1989).

[5] R. Movshovich, B. Yurke, P. G. Kaminsky, A. D. Smith, A. H. Silver, R. W. Simon, and M. V. Schneider, Observation of Zero-Point Noise Squeezing via a Josephson-Parametric Amplifier, Phys. Rev. Lett. **65**, 1419 (1990).

[6] B. Yurke, M. L. Roukes, R. Movshovich, and A. N. Pargellis, A low-noise series-array Josephson junction parametric amplifier, Appl. Phys. Lett. **69**, 3078 (1996).

[7] M. A. Castellanos-Beltran and K. W. Lehnert, Widely tunable parametric amplifier based on a superconducting quantum interference device array resonator, Appl. Phys. Lett. **91**, 083509 (2007).

[8] M. A. Castellanos-Beltran, K. D. Irwin, G. C. Hilton, L. R. Vale, and K. W. Lehnert, Amplification and squeezing of quantum noise with a tunable Josephson metamaterial, Nat. Phys. **4**, 929 (2008).

[9] N. Bergeal, F. Schackert, M. Metcalfe, R. Vijay, V. E. Manucharyan, L. Frunzio, D. E. Prober, R. J. Schoelkopf, S. M. Girvin, and M. H. Devoret, Phase-preserving amplification near the quantum limit with a Josephson ring modulator, Nature **465**, 64 (2010).

[10] C. Macklin, K. O'Brien, D. Hover, M. E. Schwartz, V. Bolkhovsky, X. Zhang, W. D. Oliver, and I. Siddiqi, A near-quantum-limited Josephson traveling-wave parametric amplifier, Science **350**, 307 (2015).

[11] L. Planat, A. Ranadive, R. Dassonneville, J. Puertas Martínez, S. Léger, C. Naud, O. Buisson, W. Hasch-Guichard, D. M. Basko, and N. Roch, Photonic-Crystal Josephson Traveling-Wave Parametric Amplifier, Phys. Rev. X **10**, 021021 (2020).

[12] N. E. Frattini, V. V. Sivak, A. Lingenfelter, S. Shankar, and M. H. Devoret, Optimizing the Nonlinearity and Dissipation of a SNAIL Parametric Amplifier for Dynamic Range, Phys. Rev. Appl. **10**, 054020 (2018).

[13] G. Butseraen, A. Ranadive, N. Aparicio, K. Rafsanjani Amin, A. Juyal, M. Esposito, K. Watanabe, T. Taniguchi, N. Roch, F. Lefloch, and J. Renard, A gate-tunable graphene Josephson parametric amplifier, Nat. Nanotechnol. **17**, 1153 (2022).

[14] J. Sarkar, K. V. Salunkhe, S. Mandal, S. Ghatak, A. H. Marchawala, I. Das, K. Watanabe, T. Taniguchi, R. Vijay, and M. M. Deshmukh, Quantum-noise-limited microwave amplification using a graphene Josephson junction, Nat. Nanotechnol. **17**, 1147 (2022).

[15] J. Shabani, M. Kjaergaard, H. J. Suominen, Y. Kim, F. Nichele, K. Pakrouski, T. Stankevic, R. M. Lutchyn, P. Krogstrup, R. Feidenhans'l, S. Kraemer, C. Nayak, M. Troyer, C. M. Marcus, and C. J. Palmstrøm, Two-dimensional epitaxial superconductor-semiconductor heterostructures: A platform for topological superconducting networks, Phys. Rev. B **93**, 155402 (2016).

[16] W. L. Sarney, S. P. Svensson, K. S. Wickramasinghe, J. Yuan, and J. Shabani, Reactivity studies and structural properties of Al on compound semiconductor surfaces, J. Vacuum Sci. Technol. B **36**, 062903 (2018).

[17] W. L. Sarney, S. P. Svensson, A. C. Leff, W. F. Schiela, J. O. Yuan, M. C. Dartiailh, W. Mayer, K. S. Wickramasinghe, and J. Shabani, Aluminum metallization of III-V semiconductors for the study of proximity superconductivity, J. Vacuum Sci. Technol. B **38**, 032212 (2020).

[18] M. Kjaergaard, F. Nichele, H. J. Suominen, M. P. Nowak, M. Wimmer, A. R. Akhmerov, J. A. Folk, K. Flensberg, J. Shabani, C. J. Palmstrøm, and C. M. Marcus, Quantized conductance doubling and hard gap in a two-dimensional semiconductor-superconductor heterostructure, Nat. Commun. **7**, 12841 (2016).

[19] W. Mayer, J. Yuan, K. S. Wickramasinghe, T. Nguyen, M. C. Dartiailh, and J. Shabani, Superconducting proximity effect in epitaxial Al-InAs heterostructures, Appl. Phys. Lett. **114**, 103104 (2019).

[20] M. C. Dartiailh, J. J. Cuozzo, B. H. Elfeky, W. Mayer, J. Yuan, K. S. Wickramasinghe, E. Rossi, and J. Shabani, Missing Shapiro steps in topologically trivial Josephson junction on InAs quantum well, Nat. Commun. **12**, 78 (2021).

[21] F. Nichele, A. C. C. Drachmann, A. M. Whiticar, E. C. T. O'Farrell, H. J. Suominen, A. Fornieri, T. Wang, G. C. Gardner, C. Thomas, A. T. Hatke, P. Krogstrup, M. J. Manfra, K. Flensberg, and C. M. Marcus, Scaling of Majorana Zero-Bias Conductance Peaks, Phys. Rev. Lett. **119**, 136803 (2017).

[22] A. Fornieri, A. M. Whiticar, F. Setiawan, E. Portolés, A. C. C. Drachmann, A. Keselman, S. Gronin, C. Thomas, T. Wang, R. Kallaher, G. C. Gardner, E. Berg, M. J. Manfra, A. Stern, C. M. Marcus, and F. Nichele, Evidence of topological superconductivity in planar Josephson junctions, Nature **569**, 89 (2019).

[23] M. C. Dartiailh, W. Mayer, J. Yuan, K. S. Wickramasinghe, A. Matos-Abiague, I. Žutić, and J. Shabani, Phase Signature of Topological Transition in Josephson Junctions, Phys. Rev. Lett. **126**, 036802 (2021).

[24] M. Aghaee, *et al.*, Inas-al hybrid devices passing the topological gap protocol, (2022), ArXiv:2207.02472.

[25] C. G. L. Bøttcher, F. Nichele, M. Kjaergaard, H. J. Suominen, J. Shabani, C. J. Palmstrøm, and C. M. Marcus, Superconducting, insulating and anomalous metallic regimes in a gated two-dimensional semiconductor-superconductor array, Nat. Phys. **14**, 1138 (2018).

[26] L. Casparis, M. R. Connolly, M. Kjaergaard, N. J. Pearson, A. Kringhøj, T. W. Larsen, F. Kuemmeth, T. Wang, C. Thomas, S. Gronin, G. C. Gardner, M. J. Manfra, C. M. Marcus, and K. D. Petersson, Superconducting gatemon qubit based on a proximitized two-dimensional electron gas, Nat. Nanotechnol. **13**, 915 (2018).

[27] D. Phan, J. Senior, A. Ghazaryan, M. Hatefipour, W. M. Strickland, J. Shabani, M. Serbyn, and A. P. Higginbotham, Detecting Induced $p \pm ip$ Pairing at the Al-InAs Interface with a Quantum Microwave Circuit, Phys. Rev. Lett. **128**, 107701 (2022).

[28] M. Pita-Vidal, A. Bargerbos, C.-K. Yang, D. J. van Woerkom, W. Pfaff, N. Haider, P. Krogstrup, L. P. Kouwenhoven, G. de Lange, and A. Kou, Gate-Tunable Field-Compatible Fluxonium, Phys. Rev. Appl. **14**, 064038 (2020).

[29] A. Kringhøj, T. W. Larsen, O. Erlandsson, W. Uilhoorn, J. G. Kroll, M. Hesselberg, R. P. G. McNeil, P. Krogstrup, L. Casparis, C. M. Marcus, and K. D. Petersson, Magnetic-Field-Compatible Superconducting Transmon Qubit, Phys. Rev. Appl. **15**, 054001 (2021).

[30] M. Xu, R. Cheng, Y. Wu, G. Liu, and H. X. Tang, Magnetic Field-Resilient Quantum-Limited Parametric Amplifier, PRX Quantum **4**, 010322 (2023).

[31] M. Khalifa and J. Salfi, Nonlinearity and Parametric Amplification of Superconducting Nanowire Resonators in Magnetic Field, Phys. Rev. Appl. **19**, 034024 (2023).

[32] W. Vine, M. Savytskyi, A. Vaartjes, A. Kringhøj, D. Parker, J. Slack-Smith, T. Schenkel, K. Mølmer, J. C. McCallum, B. C. Johnson, A. Morello, and J. J. Pla, In-situ amplification of spin echoes within a kinetic inductance parametric amplifier, Sci. Adv. **9**, eadg1593 (2023).

[33] S. Schaal, A. Rossi, V. N. Ciriano-Tejel, T.-Y. Yang, S. Barraud, J. J. L. Morton, and M. Fernando Gonzalez-Zalba, A cmos dynamic random access architecture for radio-frequency readout of quantum devices, Nat. Electron. **2**, 236 (2019).

[34] S. J. Pauka, K. Das, R. Kalra, A. Moini, Y. Yang, M. Trainer, A. Bousquet, C. Cantaloube, N. Dick, G. C. Gardner, M. J. Manfra, and D. J. Reilly, A cryogenic CMOS chip for generating control signals for multiple qubits, Nat. Electron. **4**, 64 (2021).

[35] X. Xue, *et al.*, CMOS-based cryogenic control of silicon quantum circuits, Nature **593**, 205 (2021).

[36] F. Lecocq, F. Quinlan, K. Cicak, J. Aumentado, S. A. Diddams, and J. D. Teufel, Control and readout of a superconducting qubit using a photonic link, Nature **591**, 575 (2021).

[37] L. Cochrane, T. Lundberg, D. J. Ibberson, L. A. Ibberson, L. Hutin, B. Bertrand, N. Stelmashenko, J. W. A. Robinson, M. Vinet, A. A. Seshia, and M. Fernando Gonzalez-Zalba, Parametric Amplifiers Based on Quantum Dots, Phys. Rev. Lett. **128**, 197701 (2022).

[38] T. W. Larsen, K. D. Petersson, F. Kuemmeth, T. S. Jespersen, P. Krogstrup, J. Nygård, and C. M. Marcus, Semiconductor-Nanowire-Based Superconducting Qubit, Phys. Rev. Lett. **115**, 127001 (2015).

[39] M. Veldhorst, J. C. C. Hwang, C. H. Yang, A. W. Leenstra, B. de Ronde, J. P. Dehollain, J. T. Muhonen, F. E. Hudson, K. M. Itoh, A. Morello, and A. S. Dzurak, An addressable quantum dot qubit with fault-tolerant control-fidelity, Nat. Nanotechnol. **9**, 981 (2014).

[40] K. Takeda, J. Kamioka, T. Otsuka, J. Yoneda, T. Nakajima, M. R. Delbecq, S. Amaha, G. Allison, T. Kodera, S. Oda, and S. Tarucha, A fault-tolerant addressable spin qubit in a natural silicon quantum dot, Sci. Adv. **2**, e1600694 (2016).

[41] J. Yoneda, K. Takeda, T. Otsuka, T. Nakajima, M. R. Delbecq, G. Allison, T. Honda, T. Kodera, S. Oda, Y. Hoshi, N. Usami, K. M. Itoh, and S. Tarucha, A quantum-dot spin qubit with coherence limited by charge noise and fidelity higher than 99.9%, Nat. Nanotechnol. **13**, 102 (2018).

[42] A. Noiri, K. Takeda, T. Nakajima, T. Kobayashi, A. Sammak, G. Scappucci, and S. Tarucha, Fast universal quantum gate above the fault-tolerance threshold in silicon, Nature **601**, 338 (2022).

[43] X. Xue, M. Russ, N. Samkharadze, B. Undseth, A. Sammak, G. Scappucci, and L. M. K. Vandersypen, Quantum logic with spin qubits crossing the surface code threshold, Nature **601**, 343 (2022).

[44] N. Samkharadze, A. Bruno, P. Scarlino, G. Zheng, D. P. DiVincenzo, L. DiCarlo, and L. M. K. Vandersypen, High-Kinetic-Inductance Superconducting Nanowire Resonators for Circuit QED in a Magnetic Field, Phys. Rev. Appl. **5**, 044004 (2016).

[45] J. G. Kroll, F. Borsoi, K. L. van der Enden, W. Uilhoorn, D. de Jong, M. Quintero-Pérez, D. J. van Woerkom, A. Bruno, S. R. Plissard, D. Car, E. P. A. M. Bakkers, M. C. Cassidy, and L. P. Kouwenhoven, Magnetic-Field-Resilient Superconducting Coplanar-Waveguide Resonators for Hybrid Circuit Quantum Electrodynamics Experiments, Phys. Rev. Appl. **11**, 064053 (2019).

[46] C. Eichler and A. Wallraff, Controlling the dynamic range of a Josephson parametric amplifier, EPJ Quantum Technol. **1**, 2 (2014).

[47] M. Kjaergaard, H. J. Suominen, M. P. Nowak, A. R. Akhmerov, J. Shabani, C. J. Palmstrøm, F. Nichele, and C. M. Marcus, Transparent Semiconductor-Superconductor Interface and Induced Gap in an Epitaxial Heterostructure Josephson Junction, Phys. Rev. Appl. **7**, 034029 (2017).

[48] N. Bergeal, R. Vijay, V. E. Manucharyan, I. Siddiqi, R. J. Schoelkopf, S. M. Girvin, and M. H. Devoret, Analog information processing at the quantum limit with a Josephson ring modulator, Nat. Phys. **6**, 296 (2010).

[49] X. Zhou, V. Schmitt, P. Bertet, D. Vion, W. Wustmann, V. Shumeiko, and D. Esteve, High-gain weakly nonlinear flux-modulated Josephson parametric amplifier using a SQUID array, Phys. Rev. B **89**, 214517 (2014).

[50] B. J. Chapman, E. I. Rosenthal, J. Kerckhoff, L. R. Vale, G. C. Hilton, and K. W. Lehnert, Single-sideband modulator for frequency domain multiplexing of superconducting qubit readout, Appl. Phys. Lett. **110**, 162601 (2017).

[51] B. J. Chapman, E. I. Rosenthal, J. Kerckhoff, B. A. Moores, L. R. Vale, J. A. B. Mates, G. C. Hilton, K. Lalumière, A. Blais, and K. W. Lehnert, Widely Tunable On-Chip Microwave Circulator for Superconducting Quantum Circuits, Phys. Rev. X **7**, 041043 (2017).

[52] B. J. Chapman, E. I. Rosenthal, and K. W. Lehnert, Design of an On-Chip Superconducting Microwave Circulator with Octave Bandwidth, Phys. Rev. Appl. **11**, 044048 (2019).

[53] M. C. Cassidy, A. Bruno, S. Rubbert, M. Irfan, J. Kammhuber, R. N. Schouten, A. R. Akhmerov, and L. P. Kouwenhoven, Demonstration of an ac Josephson junction laser, Science **355**, 939 (2017).

[54] A. Chatterjee, P. Stevenson, S. De Franceschi, A. Morello, N. P. de Leon, and F. Kuemmeth, Semiconductor qubits in practice, Nat. Rev. Phys. **3**, 157 (2021).

[55] M. J. Yoo, T. A. Fulton, H. F. Hess, R. L. Willett, L. N. Dunkleberger, R. J. Chichester, L. N. Pfeiffer, and K. W. West, Scanning single-electron transistor microscopy: Imaging individual charges, Science **276**, 579 (1997).

[56] S. Ilani, A. Yacoby, D. Mahalu, and H. Shtrikman, Microscopic structure of the metal-insulator transition in two dimensions, Science **292**, 1354 (2001).

[57] See the Supplemental Material at http://link.aps.org/supplemental/10.1103/PhysRevApplied.19.064032 for the raw data and the plotting code for each figure.

[58] M. Göppl, A. Fragner, M. Baur, R. Bianchetti, S. Filipp, J. M. Fink, P. J. Leek, G. Puebla, L. Steffen, and A. Wallraff, Coplanar waveguide resonators for circuit quantum electrodynamics, J. Appl. Phys. **104**, 113904 (2008).

[59] J. Bourassa, F. Beaudoin, J. M. Gambetta, and A. Blais, Josephson-junction-embedded transmission-line resonators: From Kerr medium to in-line transmon, Phys. Rev. A **86**, 013814 (2012).

[60] H. Goldstein, C. P. Poole, and J. L. Safko, *Classical Mechanics* (Pearson, New York, 2011), 3rd ed.

[61] T. A. Palomaki, J. D. Teufel, R. W. Simmonds, and K. W. Lehnert, Entangling mechanical motion with microwave fields, Science **342**, 710 (2013).

[62] L. D. Tóth, N. R. Bernier, A. Nunnenkamp, A. K. Feofanov, and T. J. Kippenberg, A dissipative quantum reservoir for microwave light using a mechanical oscillator, Nat. Phys. **13**, 787 (2017).